LA-UR- 08-7608

Approved for public release;
distribution is unlimited.

Title:	Direct observation of plasticity and quantitative hardness measurements in single crystal cyclotrimethylene trinitramine by nanoindentation
Author(s):	K. J. Ramos, D. E. Hooks, and D. F. Bahr
Intended for:	Philosophical Magazine

Los Alamos
NATIONAL LABORATORY
EST. 1943

Form 836 (7/06)

Direct observation of plasticity and quantitative hardness measurements in single crystal cyclotrimethylene trinitramine by nanoindentation

Kyle J. Ramos[a,b], Daniel E. Hooks[a,b]*, and David F. Bahr[b]

[a]*Los Alamos National Laboratory, P.O. Box 1663, Los Alamos, NM, 87545, USA;* [b]*School of Mechanical and Materials Engineering, Washington State University, P.O. Box 642920, Pullman, WA, 99164, USA*

(Received ~~31 Oct 2008~~; final version received xx Month 2008)

Investigation of deformation beginning with elasticity and continuing through the elastic-plastic transition to incipient cracking has been conducted for (210), (021), and (001) oriented single crystals of the explosive cyclotrimethylene trinitramine, commonly known as "RDX." Insturmented indentation was performed with a conical tip over a range of loads. The resulting load-depth data exhibited distinct, reproducible, orientation dependent load excursions demonstrating elastic-plastic transitions. Indent impressions were imaged by scanning probe microscopy. Impressions on the (210) and (001) planes showed deformation pileup features associated with zone axes of slip planes. Clearly discernable slip traces were evident on the (210) plane. The (021) indentations produced significant material pile-up surrounding the impression, but did not contain discrete features associable with specific zone axes. All of the orientations exhibited cracking thresholds at very low loads. The reduced moduli were anisotropic and the hardness's were isotropic indicating limited plasticity. Maximum shear stresses estimated from a Hertzian model, at load excursions, were within a factor of 10 of published shear moduli indicating deformation initiated near the theoretical yield strength presumably by homogeneous nucleation of dislocations. The material strength parameters and apparent deformation pathways inferred from this work are compared to historical microhardness testing and interpretation of anisotropic hardness in which ambiguity of results can be attributed to the effects of cracking and simultaneous slip on multiple systems.

1. Introduction

Cyclotrimethylene trinitramine (RDX) is a crystalline molecular explosive used in many types of explosive formulations. Three polymorphs have been identified. The alpha polymorph is stable in ambient conditions and crystallizes in the orthorhombic space group *Pbca* [1]. Interest in the quasistatic deformation mechanisms of this material has been motivated by efforts to understand how energy is localized during dynamic deformation to cause initiation of detonation at regions referred to as "hot spots."

It is generally accepted that initiation of detonation within energetic materials occurs heterogeneously at localized regions referred to as "hot spots" [2,3]. In plastic bonded explosives, localization has been attributed to several mechanisms, such as intergranular friction and pore collapse, which may involve crystal deformation to some extent. The mechanisms responsible for localization within energetic single crystals, free of large pores or inclusions, are unclear. Two proposed mechanisms for localization in single crystals include the formation of a dislocation pile-up that is released in a subsequent avalanche of plasticity [2,3], and the steric hindrance model that relies upon molecular shearing to account for localization [4]. There is a lack of experimental observations of elementary deformation processes in molecular crystals, at any strain rate, which makes it difficult to assess the underlying plasticity mechanisms proposed in these models. To understand deformation processes in terms of a constitutive equation based on the Orowan relation, operable deformation mechanisms, mobile dislocation densities, and dislocation velocity behavior must be known. None of these parameters have been determined with certainty for RDX.

RDX defect and deformation studies date back to the 1960's and have involved x-ray diffraction topography, etching, and microhardness indentation investigations. X-ray topography and etching have been successfully employed to characterize defect structures of as-grown crystals. Burgers vectors have been inferred by monitoring diffraction extinction as a function of the reciprocal diffracting plane vector and slip planes have been identified by etch pit alignment. Progress characterizing mechanically induced deformation has been inhibited by the brittleness of RDX. The lack of five slip systems to accommodate general strain distributions in the bulk has made indentation the predominate method to induce deformation. However, indentation investigations have been hindered due to cracking and confined plasticity adversely effecting hardness measurements and prohibiting etch pit analysis according to Amelinckxes' method [5]. This has lead to contradictory conclusions throughout literature and ambiguous slip system determinations.

RDX defect and deformation studies date back to 1969 with the solution etch pitting studies of Connick and May that suggested the primary slip plane was the (010) plane [6]. An X-ray topography study confirmed the correlation between etch pits and dislocations in these materials [7]. Microindentation studies using crystallographically oriented Knoop indentation were performed on (120), (010), and (-210) planes, from which researchers proposed an alternate {021}[100] primary slip system based upon the observed alignment of etch pits provide insight to the nature of the elastic-plastic transition. A significant variation of hardness (300-700 MPa for the (-210) plane) was noted as a function of orientation with respect to the long axis of the indenter. Subsequent tests using Vickers microindentation on {210}, (001), and (111) planes confirmed the 390 MPa hardness [8]. This study contradictorily concluded that the originally proposed (010) plane was the primary slip plane, while slip on the (011) or (021) planes were

considered not well defined based on etch pit alignments. Both of these studies were conducted with 500 mN loads that produced significant cracking around the indenter. Preferential cracking on the (00-1), (24-1), and (241) planes was promoted by the orientation of the Knoop indentation [9]. Although not observed, cross-slip was suggested between the (010) and (021) systems as the [-100] direction is common to the (021), (02-1), and (010) planes. In addition the possibility of ±[01-2] slip was suggested for the {021} plane based on geometric consideration of intermolecular displacements. Orientation dependant Knoop hardness tests on the (210) plane with 150mN loads showed hardness variation of 320-440 MPa [10]. The variation of hardness as a function of orientation was analyzed using the effective resolved shear stress model proposed by Brookes and O'Neill [11], and agreement of hardness variation was only achieved when slip was assumed to occur simultaneously on the {021}[100] and (010)[001] systems. Etch pit analysis using Amelinckxes' method was precluded by the spatially confined plasticity in RDX, which produced overlapping, ill-defined etch pits without the appearance of slip traces [5]. Cracking and confined slip made the results from the Knoop hardness tests less definitive than tests conducted on more ductile molecular cyrstals, such as pentaerythritol tetranitrate [10].

There are many similarities among the previous microindentation results, but the differences between suggested slip systems and material strength parameters in RDX have not been resolved. The reason for the differences may be attributed to the use of different loads, and especially, induced cracking in RDX, which naturally affects hardness and etching results.

A number of x-ray topography studies have characterized the microstructure of as-grown single crystals of RDX [7,9,12-14]. Crystals grown from acetone were found to contain dislocation densities of 10 to 10^3 lines per cm^{-2} and growth sector boundaries with a typical strain of 10^{-5} [12]. Bulk defects, such as solvent inclusions, were shown to serve as origination sites for dislocations as indicated earlier by Gross and similarly confirmed in other materials [15,16]. Possible burgers vectors were identified by monitoring diffraction extinction as a function of the reciprocal diffracting plane vector [13,14]. Unfortunately x-ray topography could not be employed to characterize mechanically induced deformation due to the confined nature of plasticity within RDX.

The purpose of this study is to apply nanoindentation and post-indentation microscopic characterization to RDX single crystals to investigate plasticity and resolve contradictory conclusions in literature. Deformation studies at the length and loading scales used in nanoindentation allow for the deconvolution of brittle failure and plastic deformation mechanisms that are most often intertwined at larger scales for molecular crystals [17]. With indentation loads 100 to 1000 times lower than previous micro-indentation experiments, elastic-plastic behavior can be observed without the complication of cracking. Topographic post-characterization of indent regions in brittle materials, such as MgO, has demonstrated the potential to resolve deformation features with greater resolution than previously achieved in molecular crystals [18]. The experiments in the current study are intended to demonstrate the capability and extent to which plasticity can be quantified in brittle molecular crystals using these techniques. It is envisaged that increased capability and understanding to investigate deformation processes within molecular materials will benefit not only the explosives industry but the pharmaceutical and optoelectronics industry as well.

2. Materials and experimental methods

2.1 *Crystal growth and surface preparation*

All crystals used in this study were grown from unseeded solutions of RDX and acetone at either ambient temperature or 32° C. UK manufactured RDX (Woolwich process) was dried, purified by Soxhlet extraction in acetone, and recrystallized in acetone prior to use. Slightly undersaturated solutions were placed in either 100 mL flat-bottom vials or 1000 mL tall, spoutless beakers partially sealed with parafilm coated coverings. The bottom 1/3 of the beakers was immersed in a temperature controlled thermal ballast bath while the tops were open to air at ambient temperature. This method allowed for convective mixing that caused continuous reflux, washing the beaker sides and preventing parasitic growth. The solutions were allowed to slowly attain supersaturation in a period of several weeks upon which crystals spontaneously nucleated and were allowed to grow to ~2-7 mm in extent over an additional period of several weeks. Crystals were harvested from beakers by reducing the temperature to ambient conditions over an extended period and exchanging the solutions with deionized water. The harvesting method was required to avoid thermally induced cracking due to temperature differences from the solution or cooling due to rapid evaporation of acetone from crystal surfaces. Solutions in flat-bottom vials were allowed to evaporate completely before harvesting crystals, avoiding the complications associated with harvesting from solution.

Once RDX crystals were obtained, habit planes were selected and indexed for indentation. A Huber optical two circle reflection goniometer was used to measure interfacial angles and index planes by redundant reference to crystal facets. Crystals of the equant and prismatic morphology were obtained, typically possessing ~16-30 facets [6]. The surfaces of crystals harvested from solution were typically covered by small crystallites to varying degrees depending upon the care taken during solution/water exchange. These crystals had to be solution washed. For quality data, nanoindentation requires extremely pristine, flat and smooth surfaces. As a guide, surface roughness should be much (several orders of magnitude) less than the contact heights involved in the experiments to ensure that the ideal configuration of a paraboloid of revolution normally loaded into a flat, infinite half-space is approached. It was determined that acceptable regions within habit planes could be obtained by short period washings in solutions of varying concentrations of acetone and water. {001} planes were most easily obtained by this method and could withstand washing in pure acetone producing apparent layer by layer dissolution. All other planes observed were etched to ruin with pits extensively covering the surface when washed for the shortest periods in pure acetone (The etch pit observations made by Connick and May were confirmed [6].). Partially RDX saturated acetone/water solutions were observed to be most successful for preparing other planes when washing was required. {001} planes and regions within {210} planes were the only indentation samples successfully prepared by solution washing. The flattest, smoothest habit planes were obtained for the crystals grown in the flat-bottom vials wherein the solution was allowed to completely evaporate. It seems possible to obtain acceptable planes for indentation from any plane having sufficient reticular area contained in a given morphology.

Successfully prepared samples were mounted to ferrous metal specimen disks with a minimal amount of cyanoacrylate glue. Once mounted to the disk, the indentation plane of the samples was investigated with an optical microscope for parallelism with a single focal plane. The samples were swept through the field of view of a microscope at magnifications from 500 to

1,000 with a micrometer to ensure sample tilt of less than 1-3° prior to indentation. This tilt was later verified by atomic force microscopy (AFM). Only samples with parallel surfaces were selected for indentation to avoid the deleterious effect of non-orthogonal indentation. AFM assessment of each sample was performed because it was determined that subtle features of surface roughness not obvious from scanning probe microscopy (SPM) average roughness (R_{ave}) and root-mean-square roughness (R_{rms}) measurements made with the indentation tip had a substantial effect on data. Table 1 summarizes the variety and condition of samples tested and presented in this study.

2.2 *Indentation & topography characterization*

Nanoindentation was performed using a Hysitron TriboIndenter® equipped with a low load QSM transducer (Minneapolis, MN). Indentations were carried out with a 90° conical tip having an effective radius, R, of 1,482±90 nm on the surfaces indicated in Table 1. The tip radius was determined from elastic loading experiments on fused quartz in which an effective radius of curvature was fit to the data according to the Hertzian loading profile [19]. This tip provided the ability to perform semispherical indentation upon initial loading and a suitable resolution for imaging indentation impressions by SPM immediately following unloading. Indenter-tip SPM imaging of surfaces was conducted immediately prior to indentation to ensure that relatively smooth, defect-free regions were selected for indentation, to assess surfaces for residual deformation, and establish the orientation of deformation features. Further topographical characterization was performed with AFM using a Veeco di CP-II® with a 100 μm scanner in intermittent-contact mode, wherein the drive frequency was chosen on the low frequency side of the main resonance peak in the cantilever response curve (Veeco cantilever model: MPP-31123-10).

<Table 1>

3. Results

3.1 *Load-depth response*

Load–depth curves taken on the (210), (021), and (001) orientations are shown in Fig. 1. Well-defined indentation impressions possessing repeatable form were produced by at least 50 indents on each of the surfaces, employing multiple samples. Indentation was initially conducted over large load ranges (.25-10 mN) to establish ranges over which deformation behavior was of interest for each orientation. Several important features in these curves are the substantial load excursions, the presence of creep at the maximum load, and the small degree of elastic recovery upon final unloading.

<Figure 1>

The reduced elastic modulus and hardness were calculated from the load-depth curves using the unloading slope method described by Oliver and Pharr [20]. A first order estimate of the maximum shear stress under the indenter tip was calculated at load excursions assuming a Hertzian pressure distribution [21]. The resulting values for reduced elastic modulus, hardness,

and maximum shear stress for each of the orientations are given in Table 2 and 3. The reduced modulli were distinctly anisotropic; whereas, the hardness and maximum shear stress values were nearly isotropic. The hardness and shear stress values were approximately equal indicating hindered dislocation mediated plasticity. The values obtained for reduced modulus were consistent with previous determinations of the elastic tensor of RDX by resonant ultrasound spectroscopy (RUS) and Brillioun spectroscopy [22,23]. The trend of $E_r^{(210)} > E_r^{(021)} > E_r^{(001)}$ is consistent with $c_{11} > c_{22} > c_{33}$. The values obtained for hardness were consistent with the determinations by Elban et al. [9,24] while significantly greater than those made by Halfpenny et al. and Gallagher et al. [8,10].

<Table 2>

When indentations were carried out on habit planes containing surface asperities (>1-3 nm in height) with spacing comparable to the contact radius '*a*', load-depth curves were purely plastic containing no load excursions. Surfaces had to be carefully prepared and characterized by imaging prior to indentation to ensure that surface asperities did not interfere with measurements. Characterizing the surface via AFM was important as asperities, significant enough to affect the appearance of repeatable load excursions Fig. 2(a, d, g), oftentimes could not be adequately observed while scanning with the indenter tip. This result is consistent with previous work, wherein electropolishing of metals was necessary to obtain data with distinct elastic-plastic behavior [25]. Within this study it was observed that unacceptably rough surfaces prepared by different means produced load-depth curves with load excursions occurring over a spectrum of loads with varying displacements. Therefore it was important to ensure the quality of the surface contacted by the indenter if the defect nature of the specimen were to be inferred.

Using the loading sequences shown in Fig. 2(b, e, h), partial unloading segments demonstrate that the initial loading was purely elastic as the material loaded and unloaded along the same paths depicted in Fig. 2(c, f, i). As a first order estimate, the Hertzian contact model consisting of a sphere making purely elastic contact with an elastically isotropic half-space can be used to analyze the observed initial loading behavior [19]. The initial loading portions of the curves were analyzed using the load-displacement relation for a Hertzian contact:

$$P = \frac{4}{3} E_r \sqrt{R} \delta^{3/2} \tag{1}$$

where P is the applied load, δ is the penetration depth, R is the tip radius (if the sample is flat), and E_r is the reduced elastic modulus, which can be related to the elastic modulus, E, and Poisson's ratio, υ, of the sample (s) and indenter (i) with:

$$\frac{1}{E_r} = \frac{1-\nu_i^2}{E_i} + \frac{1-\nu_s^2}{E_s} \tag{2}$$

The elastic penetration produces an indenter/sample interface described by the contact radius, a:

$$a = \sqrt{\delta R} = \left(\frac{3PR}{4E_r}\right)^{1/3} \tag{3}$$

This contact gives rise to an analytic stress field under the indenter: Hertzian pressure distribution. The maximum pressure 'P_{max}', principle shear stress 'τ_{max}', and tensile stress '$\sigma_{r\text{-}max}$' are respectively located at the point of axial symmetry on the surface/ indenter interface, *0.48*a* below the previous point (assuming $\upsilon = 0.3$), and on the contact perimeter of the surface/indenter interface. Of these stresses τ_{max} and $\sigma_{r\text{-}max}$ contribute most to shear deformation by slip as P_{max} is mostly hydrostatic. At their respective maximums τ is a factor of approximately two greater than σ_r, indicating that yielding should be expected to initiate below the sample surface at a principle shear stress given by:

$$\tau_{\max} = \frac{1}{2}\left|\sigma_z - \sigma_\theta\right| = 0.31\left(\frac{6E_r^2}{\pi^3 R^2}\right)^{1/3} P^{1/3} \tag{4}$$

<Figure 2>

As shown in Fig. 2(c, f, i), the initial loading does follow Eq. (1) demonstrating agreement with the Hertzian contact model, which, when coupled with the load–unload overlap, further verifies the use of elastic contact mechanics for the initial loading portion of the indentation. The respective reduced elastic moduli, deduced from the conical indenter, were used for analyzing the different indentation planes. The indentations were separated by at least 50 μm, which was much greater than the contact radii, ensuring that each subsequent indentation was not deleteriously effected by previous indents. Typical load-depth responses for varying quality specimen distinguished material by processing method. While as-grown samples displayed highly reproducible load excursions, samples processed by thermal or mechanical cleavage displayed a varied response with excursions occurring over a wider range of loads, without ever reaching the excursion loads observed for pristine samples. We surmise that this varied response is an indicator of relative dislocation density in the sample. Here, we present only the reproducible load excursion behavior observed on pristine samples; the varied results from differently processed samples will be the subject of a future report [26]. Table 3 summarizes the anisotropic excursion behavior.

<Table 3>

3.2 Indent impression topography

Deformation topography around impressions was observed by scanning probe microscopy (SPM) following indentation. This was initially accomplished by contact scanning

with the indenter tip using the Hysitron instrument (SPM). It was noted upon subsequent imaging with AFM that indenter tip SPM did damage some surface features even at very low contact forces. Following this observation all surface topography measurements were made with both techniques, but on separate indents. All images presented here were acquired within 24 hours following indentation. There was no noticeable change in impression appearance within this time period. Subsequent images taken three to four days later revealed that surface deformation around the indent impressions changed as a function of the time elapsed after indentation. The change was quite pronounced after a month. This was evidence of appreciable residual stresses and molecular mobility that may occur at high homologous temperatures (T_h = 298K/478K = 0.62).

Anisotropic deformation features within the pile-up surrounding impressions were observed within micrometer sized SPM/AFM images. These features were consistent with the crystal symmetry of the indentation planes and required indexing (Note the two-fold symmetry exclusive to the deformation of the (001) indentation plane, Figure 5.). A procedure had to be developed to index nanometer dimensioned features with respect to crystallographic references provided by zone axes defined by intersecting indentation and habit planes observable on the millimeter size scale. To develop this procedure reference frames of the nanoindenter, AFM, and optical microscope had to be correlated. Angular displacements between indentation array coordinates, SPM scanning coordinates, and the orientation of reference zone axes defined by intersecting crystal planes were measured for each sample. With these measurements, prominent deformation features within SPM images could be indexed with respect to zone axes defined by intersecting crystal planes. Once a relationship between prominent deformation features and reference zone axes were established, the orientation of subsequent AFM images was known.

Projections of deformation zone axes upon indentation planes were generated to interpret the deformation features within oriented SPM/AFM images. This was accomplished by transforming Miller indices from the reciprocal basis to an orthonormal basis to obtain unit normals, taking the cross product of the normals to identify zone axes, and transforming/rotating the zone axes into a two coordinate reference frame so they could be plotted in polar coordinates. This procedure was conducted such that the unit normals of the (210), (021), and (001) indentation planes were oriented coincident with the z-axis and the reference zone axes used to orient SPM and AFM images were coincident with the zero angular position in polar coordinates. Zone axes associate with known/suspected deformation mechanisms were included in the polar plots and subsequently overlaid digitally upon SPM and AFM images that had been rotated such that reference zone axes were coincident within the images. The deformation mechanisms used to construct the polar plots are listed in Table 4.

<Table 4>

The correlation of reference frames between the nanoindenter, AFM, and optical microscope were possible within 1-3 degrees of uncertainty. This small amount of quantifiable misorientation offers reassurance that the compound images can be used to interpret deformation features. Most of this uncertainty was caused by misorientation of the nanoindenter's XYZ axes motorized staging system, producing the alignment of indent arrays, and the scanning direction of the three-axis piezo positioner (Triboscanner®) during SPM. An array of indents could be

performed and imaged with SPM as a whole to ascertain the misorientation and eliminate its contribution to the angular uncertainty. This calibration procedure had to be repeated every time the transducer was removed from the three-axis piezo positioner (Triboscanner®) as the amount of angular misoreintation changed with slight mounting differences as the transducer was reinstalled in the double-dovetail groove.

These compound images composed of SPM/AFM data and projections of deformation zone axes expedite the interpretation of deformation features. The most obvious benefit of the compound images is that deformation features consistent with known or suggested deformation mechanisms can be identified from direct comparison. Another benefit is that the known or suggested deformation features can be compared to observations as a group on each indentation plane such that small error in indexing SPM/AFM images are easily recognized and the indexing of multiple features as a group is self-consistent. For observation of deformation features inconsistent with known deformation mechanisms, the angle between the feature and a reference zone axis can be read off the plot. Using the indentation plane unit normal, the reference zone axis, and the angle read from the plot a system of four equations can be formed using the vector and scalar products to calculate the zone axis coincident with the deformation feature. If an inexplicable feature is observed on two other indentation planes the procedure can be repeated. If the zone axes are consistent with a single plane, the plane associated with the deformation mechanism can be presumptively determined.

An indenter tip SPM image of an impression on (210) planes is presented in Figure 3. AFM images of fresh indents on this plane are shown in Figure 4 displaying complex anisotropic deformation. Slip traces and a crack paralleling zone axes consistent with {011} and (010) slip planes and an anisotropic (001) cleavage plane are discernable. The slip traces consistent with (010) slip are less discrete, composed of smaller and less distinct steps, and appear to become more prominent in height images as pile-up along this zone axis increase as a function of indentation load (The green line indicates this feature in the deflection image.). Slip traces consistent with {011} slip are prominent close to the top and bottom of the impression indicating the symmetry related slip systems were operable during deformation. Away from the impression, only one of the systems appear to have been operable above and below the impression; however, at the end of these slip traces both systems are evident on single traces (indicated by A arrows). Faint slip traces are also perceptible on the right side of the impression. These features are interesting as they have an opposite slope as compared to the prominent (011) traces and they are consistent with slip on the (02-1) slip plane (indicated by B arrow).

<Figure 3>
<Figure 4>

Indenter tip SPM images of impressions in (001) oriented RDX samples at several maximum indenter loads are presented in Figure 5. The indent impressions from a conical tip are pyramidal at low loads, and transition to conical at higher loads, presumably as slip accommodates the geometrically necessary deformation imposed by the contour of the tip. This appears to be a direct demonstration of compatibility conditions in a material with few slip systems. Figure 6 illustrates a side-by-side comparison of (001) RDX and aluminum impressions at similar contact depths. A pair of sides bounding the pyramidal impressions are

consistent with (010), {011}, and {021} slip systems. The pile-up along these sides bow out with modest increases in indentation load whereas the other sides paralleling the (100)X(210) zone axis remain straight. The evolution of impression shape is accompanied by radial or median type cracking, that first appears at a 3 mN indentation load, parallel to the (111)X(001) zone axis and progresses to the appearance of lateral cracks around the indent impression at higher loads. Unfortunately, AFM images were acquired after the impressions were imaged with the indenter tip. Fresh indents have not been produced for direct AFM imaging because of the difficulty in preparing samples with this plane suitable for indentation. Judging from AFM images of slip traces partially damaged by indenter tip SPM imaging, clear AFM images of fresh indents will reveal complex slip traces as observed on the (210) indentation plane.

<Figure 5>
<Figure 6>

An AFM image of an impression on an (021) oriented RDX sample is presented in Figure 6. The impression is somewhat nondescript, with a conical impression and comparable plastic pileup to the other orientations but no apparent slip traces. Alignment of the crack and pile-up is consistent with the (100) plane suggesting cleavage accompanied by deformation that is not clearly associable with any known or suspected slip system. In this orientation the (010), (02-1), and {011} zone axes are all coincident. A low cracking threshold (< 1.5 mN) was observed.

<Figure 7>

4. Discussion

Nanoindentation has proven to be an effective technique for investigating dislocation mediated plasticity in brittle molecular single crystals. Many traditional techniques, imposing more simple states of stress, have been employed with limited success. The inapplicability of uniaxial tension and compression tests to investigate more than elastic-brittle responses in cases of arbitrarily oriented crystals has been demonstrated [3,27,28].

Many molecular crystals have low symmetry and possess few slip systems. The well established continuum mechanics principle of material compatibility requires that a simply connected solid must be able to deform along five unique directions to accommodate general strain distributions in the bulk and remain simply connected [29,30]. In crystalline materials this requirement dictates five unique slip systems; this requirement is relaxed in complex ways near free surfaces [31]. At a free surface, compatible movement of half the space found in the bulk is not required. In the case of uniaxial compression tests, confining boundary conditions are imposed by platens such that the relaxation of material compatibility requirements at the specimen surface are no longer valid. This illustrates the advantage of indentation. Contact areas are minimized, imposing the least restrictive boundary conditions as deformation is investigated at the surface where dislocation mediated plasticity can occur prior to brittle failure, even though there are generally less than five available slip systems. This capability is gained in

exchange for increased complexity of deformation stress states and interpretation of results. Thus, elementary deformation mechanisms *can* be extracted from observation of residual surface features, but complex features can preclude specificity.

Investigation of deformation beginning with elasticity, through the elastic-plastic transition, and to incipient cracking has been conducted for the (210), (021), and (001) orientations of single crystal RDX. Topographic data was obtained using SPM with the indenter tip and AFM to interpret deformation in terms of both the load-depth curves from instrumented indentation and features produced by operable slip systems. Microscopic features with height dimensions on the nanometer scale were crystallographically indexed in a consistent manner so that deformation mechanisms could be inferred. Consideration was given to the fact that inferences of slip planes could not be assessed further without appearance of the same deformation mechanism on multiple indentation planes. Combining the topographic and load-depth curve observations allowed for a fuller assessment of dislocation mediated plasticity within RDX.

The load excursions in the load–depth curves, shown in Fig. 2(a, d, g), indicate a transition between elastic and plastic deformation. When metals and ceramics with low dislocation densities are subjected to nanoindentation, the "pop in" [32-34] or "excursion" [19,35] behavior is often correlated to either the nucleation of dislocations in a perfect crystal or the rapid multiplication of dislocations from a limited source population. Early observations of load excursions in metal crystals promoted the concept of dislocations by noting that yielding was observed near the theoretical shear strength of the perfect crystal [36]. This was interpreted as indication that homogeneous nucleation of dislocations was occurring. In an ideally isotropic material, the principle shear stress obtained from the Hertz model can be equated to the critically resolved shear stress which provides a direct measure of the theoretical shear strength. Crystalline RDX is distinctly not an elastically isotropic material. The use of the Hertz model and similar theoretical shear strength arguments here pose questions regarding validity.

The initial loading portion of load-depth curves were demonstratively elastic allowing for the use of elastic contact mechanics in analysis. An isotropic model, the Hertz model in conjunction with the Oliver and Pharr method to obtain reduced moduli, was used to obtain a first order estimate of the maximum shear stress under the indenter tip. The agreement in fitting to Eq. (1) is sufficiently satisfying. However, it merits scrutiny as the boundary conditions for the underlying axi-symmetric pressure distribution satisfying the biharmonic equation are not met because of elastic anisotropy of RDX [37]. The (001) normal coincides with a two-fold symmetry axis whereas the (210) and (021) do not. The best agreement is demonstrated for the (001) load-depth curve in Fig. 2(i). As expected, the agreement worsens for indentations on planes with lower symmetry. An anisotropic analysis of the elastic contacts formed with RDX will be considered in a future publication to deduce the reduced moduli and FEA derived stress distributions from known elastic constants [38,39].

The maximum shear stress values, ascertained using the Hertz model, are within a tenth of the measured shear moduli. If these values are assumed to be indicative of critically resolved shear stresses, they indicate yielding occurred near the theoretical shear strength presumably by homogeneous nucleation of dislocations. The presumption of homogeneous nucleation of dislocations is primarily based upon extensive observations that have been made in metals. The fact that the behavior of the load excursions was extremely repeatable for each orientation,

within load-depth curves produced from indents on individual samples and multiple different samples, indicate that a fundamental material phenomenon was occurring. It would be rather difficult to imagine that separate samples from different growth runs had exactly appropriate limited dislocation source populations to produce the repeatable behavior observed. The loads and displacements in Table 3 represent the largest values observed. As these values were never eclipsed, even after multiple samples had been tested for each orientation, they are interpreted as limiting values associated with the occurring phenomenon.

This phenomenon could alternatively be interpreted in terms of homogeneous rather than heterogeneous nucleation. It has been demonstrated that quantitative evaluation of homogenous dislocation nucleation assertions can be performed by statistical analysis of qualitatively similar data [34]. Such an analysis might provide insight to the nature of the elastic-plastic transition presented here, but would involve significant additional effort in both extending the approach to anisotropic systems and acquiring sufficient data for meaningful statistics. For the cases involving pristine as-grown crystals presented here, this approach is deemed unnecessary because the orientation dependent load-excursions were both highly repeatable and were qualitatively quite different. Such an approach may be useful in the future or for statistically interpreting the affects of pre-existing defect structures, because load excursions have shown greater stochastic variation following sample processing.

The topographic images are the only readily apparent means to ascertain what deformation mechanism corresponds to the phenomenon occurring at load excursions. The resolution of past x-ray topography and etching studies of dislocation mediated plasticity in molecular materials with hindered plasticity has been inadequate to distinctly determine deformation mechanisms. The ambiguity associated with the low resolution has been a major difficulty. The indenter tip SPM and AFM images presented in this work have promising resolution. The appearance of cracks as a function of indenter load, listed in table 3, indicate that the excursions are probably not associated with crack initiation. The (210) AFM image indicates anisotropic deformation occurred on planes consistent with {011}, {021}, and (010) slip in a complicated manner. The load dependence of pile-up along the (010) zone axis, the apparent presence of {011} slip on single slip traces, and the deviation of {011} slip traces from a line suggest deformation mechanism changes. This is further supported by indenter tip SPM images from (001) impressions which showed anisotropic bowing with a modest increase in load of the pile-up features initially parallel to the zone axis shared by the (010), {011}, and {021} planes. Cross-slip of dislocations amongst the slip systems could be responsible for these behaviors. This explanation has previously been suggested by Elban, et al [9]. It was noted that the [100] slip direction, conjectured from x-ray topography of the post-growth motion of dislocations [13], is contained in (010) and {021} planes providing the necessary condition for cross-slip. The occurrence of slip on multiple slip planes, suspected deformation mechanism changes, and inadequate topography information from three different orientations prohibits the unambiguous determination of slip planes associated with deformation mechanisms and their contribution to the load excursion behaviors. However, if an inference is made based on the order of appearance of slip traces the {011} planes could be associated with the dominate slip system and the load excursion observed for (210) indentation.

The current observations resolve the apparent differences in reported microindentation investigations in literature. Slip traces consistent with slip on {011}, {021}, and (010) planes

were observed in an AFM image of a single (210) indent impression. This is a prominent plane in the morphological habit of RDX, grown from acetone, and has received extensive investigation in microindentation studies. Elban et al [24,40] and Halfpenny et al [8] have disagreed about determinations of dominate slip planes, and Elban et al [9] have cautioned against attempting anisotropic hardness interpretations such as the one conducted by Gallager et al [10]. In light of the present results, the disagreement associated with dominant slip systems and how well-posed anisotropic hardness interpretations might be for RDX are understandable. The determination of the dominate slip system was dependent upon the resolution and interpretation of etching and presumably the load at which indentation was conducted. In the present experiments slip traces associated with different zone axes appeared as a function of load and became inter-dispersed spatially with increasing loads. This would make interpretation of etch pits to identify a dominate slip systems very difficult, even if well resolved etch pits were achieved at the micrometer scale. Past efforts to interpret anisotropic hardness measurements in terms of slip systems, using the Brookes or Daniels et al type models [11,41], have demonstrated that deformation must be accommodated by simple slip, cracking must not convolute hardness measurements, and Amelinckx's method of etch pit analysis must be possible in order to attain meaningful results [5,42]. Unfortunately, none of these criteria are even nearly met for indentation on the (210) RDX plane.

5. Conclusions

Load-depth curves have been recorded for (210), (021), and (001) planes of RDX by nanoindentation. Distinct, reproducible, orientation-dependent load excursions were observed. The load excursion behavior was dependent upon surface contact quality and material defect content, indicating that the technique maybe used to distinguish samples according to relative dislocation densities. Hardness and reduced modulus values determined from the data are consistent with previous literature. Estimation of resolved shear stresses and comparison to hardness values suggests that RDX dislocation mediated plasticity is hindered. Post-characterization of the surface topography surrounding indent impressions confirms previously determined slip systems, suggests complex deformation mechanisms such as cross slip among several slip systems and clarifies previous ambiguity regarding slip system dominance. Cracking was observed in all orientation at low loads, consistent with limited plasticity.

In future work it will be possible to determine the distribution of shear stresses under the indenter tip with continuum modeling just prior to the observed load excursions. This will allow the correlation of zone axes, associated with observed slip traces, with resolved shear stresses on proposed slip systems and replace isotropic approximations used in this report. In order to unambiguously determine slip direction for completing slip systems, further indentation on other orientations and post-indentation etching and microscopy will be required. Thermal etching in artificial atmospheres to increase the vapor pressure of RDX crystals is being undertaken to employ Amelinckx's etch pit analysis technique on the nano-micrometer scale in a similar manner as performed by Gaillard et al. [5,18,43,44]. The experimental configuration is amenable to molecular dynamics simulations, and it is hoped that such simulations employing fully flexible potentials might allow direct visualization of operable mechanisms responsible for the load excursions and topographic deformation features observed.

Finally, given the success in obtaining discrete, reproducible, quantified strength properties, and in some cases resolving zone axes of slip planes directly, it is hoped that this technique will be more broadly applied to structurally dependent deformation studies of this class of materials. Guidelines for the mechanics of molecular materials, including the relative importance of symmetry and lattice-deduced pathways, molecular flexibility, and chemical interaction would greatly assist efforts in the explosive, pharmaceutical, and emerging optoelectronics industry.

Acknowledgements

This work was supported by the National Nuclear Security Administration Science Campaign 2, and the Office of Naval Research. This work was performed, in part, at the Center for Integrated Nanotechnologies, a U.S. Department of Energy, Office of Basic Energy Sciences user facility at Los Alamos National Laboratory (Contract DE-AC52-06NA25396). We are grateful to Greg Swadener, Marc Cawkwell, Tommy Sewell, and Geoff Brown for helpful conversations.

Table Captions:

Table 1. Summary of faces indented

Indentation Plane	Surface Condition			
	Growth & Preparation Method	*Slope* (°)	*Roughness* R_{rms} (nm)	*Roughness* R_{ave} (nm)
(210)	B ‡	0.9	1.25 - 4	1.0 - 3.4
(021)	B ‡	2.1	1.1 - 4	1.3 - 2.8
(001)	A	1	2.2 - 3.2	1.8 - 3.4

A = growth from 1,000 ml beaker with solution wash as described in the text
B = growth from vial wherein solution was allowed to completely evaporate as described in the text
‡ The roughness values are inflated due to the presence of widely spaced growth steps. The larger rms values indicate this as the large deviations from the average height, due to the growth steps, are weighted more heavily by the squared dependence. Indentation was conducted well between the steps at locations with roughness more adequately represented by the minimum values listed

Table 2. Reduced elastic modulus and hardness with standard deviations.

Indentation Plane	Er (GPa)	H (MPa)
(210)	21.0 ± 0.6	672 ± 35
(021)	18.2 ±. 0.6	681 ± 33
(001)	16.2 ±. 1.0	615 ± 35

Table 3. Summary of anisotropic load excursion behavior and cracking with standard deviations

Indentation Plane	Excursion Behavior					Cracking ♦ Threshold P_c (mN)
	Load (μN)	$\Delta\delta$ (nm)	Δt (ms)	*a* (nm)	τ_{max} (MPa)	
(210)	246±42	17±4	1.55±0.3	236±14	645±37	.8≥ P_c >.5
(021)	368±57	24±5	2.5±0.4	287±16	658±40	1.5≥ P_c >1
(001)	994±94	79±7	2.1±0.5	407±13	885±36	4.6≥ P_c >3

♦ This is the cracking threshold as assessed by AFM and optical observation at 1000X.

Table 4. Summary of known/suspected deformation mechanisms used to construct zone axes projection figures

Deformation Plane	Interpretations in Literature
(100), (010), (001)	Cleavage Planes[a]
(241), (24-1)	Crack Planes[e]
(010)	(010)[001] Slip System[a, b, f]
(011), (0-11)	{011}[100] Slip System[b, e, f]
(021), (02-1)	{021}[100] or {021}±[012] Slip Systems[b, c, d, e, f]

[a]Reference [6].
[b]Reference [14].
[c]Reference [24].
[d]Reference [8].
[e]Reference [9].
[f]Reference [10].

Figure Captions:

Figure 1. Typical load-depth curves for the indentation of RDX: (210), (021), (001)

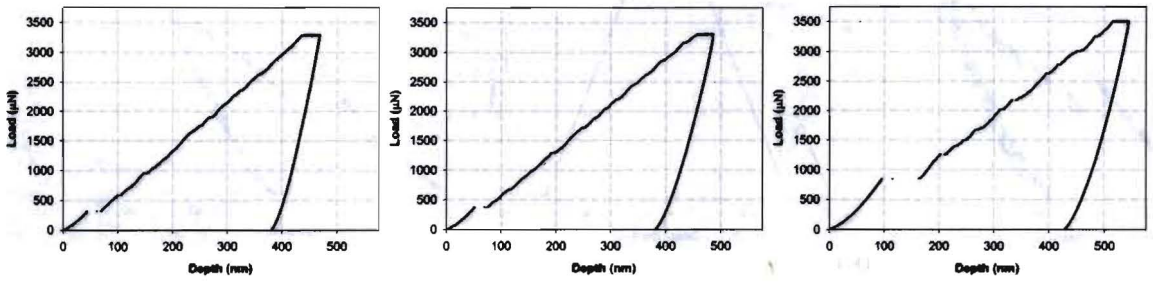

Figure 2. Load-depth data sequences illustrating repeatable load excursion, loading profile with partial unloading segment to assess the degree of elasticity, associated load-depth curve: (210) a-c, (021) d-f, (001) g-i

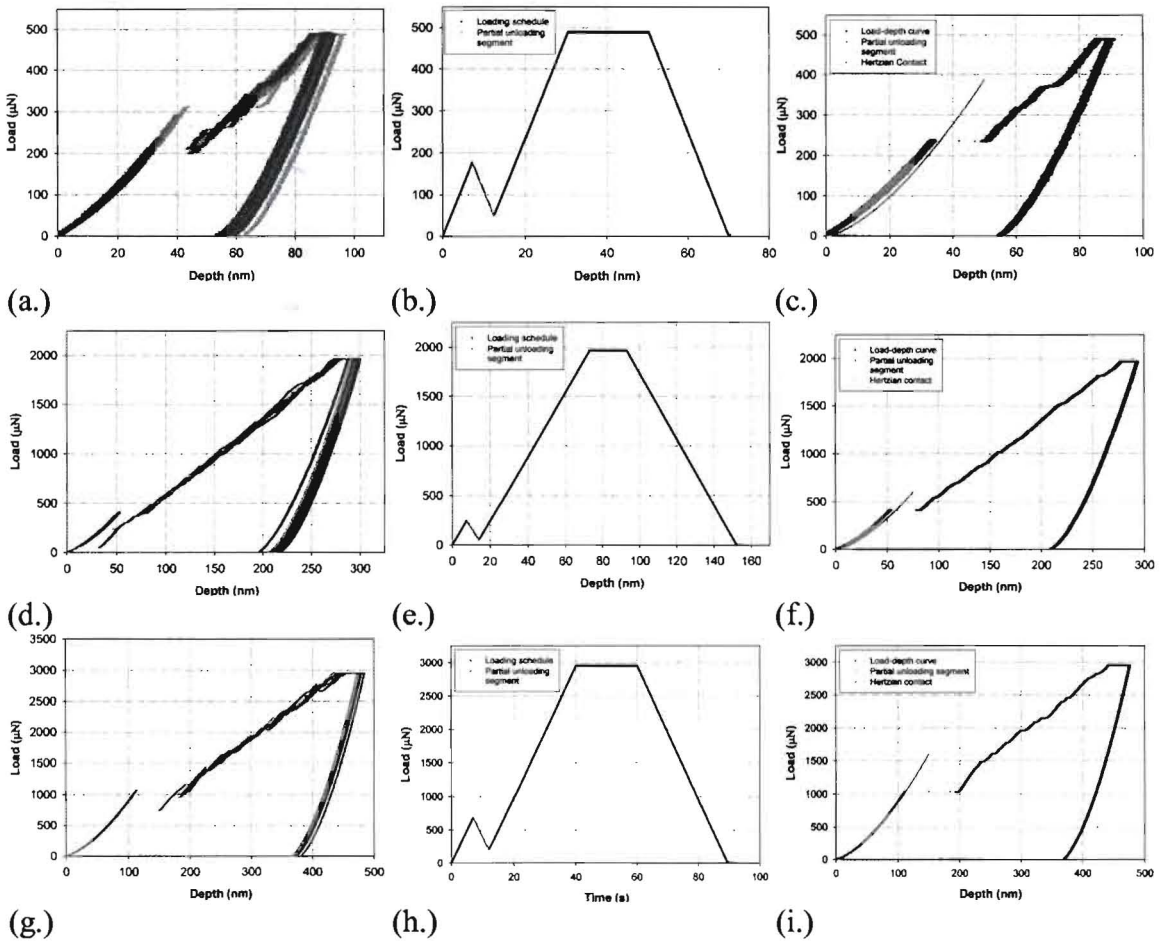

Figure 3. indenter tip SPM deflection image of an (210) impression (6.2 mN load, 10 μm image).

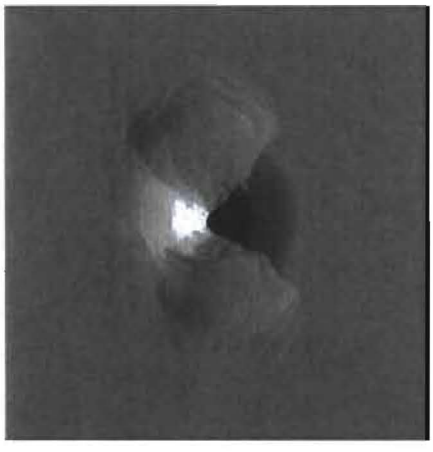

Figure 4. AFM image of (210) impressions: 12 μm images of 6.7 mN indent (a.) height contrast 0-291 nm (b.) deflection image with project zone axes overlaid and 5.3 mN indent (c.) height contrast 0-135 nm (d.) deflection image with project zone axes overlaid.

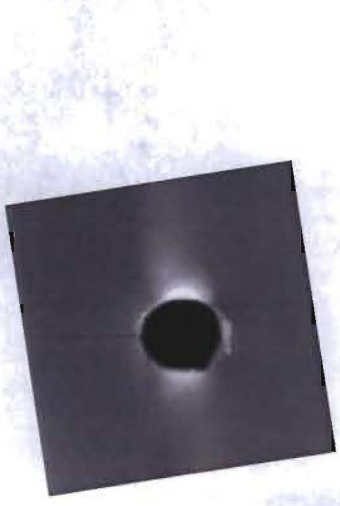

(a.)

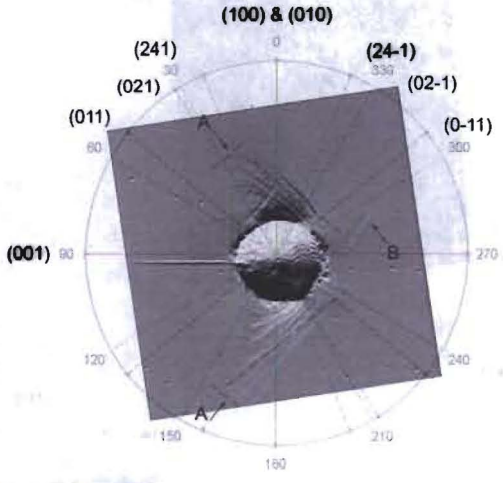

(b.)

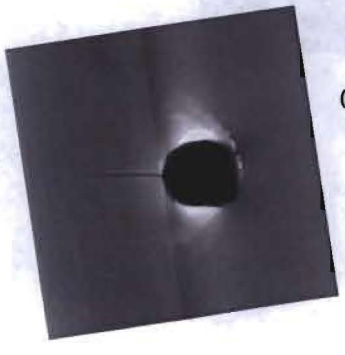

(c.)

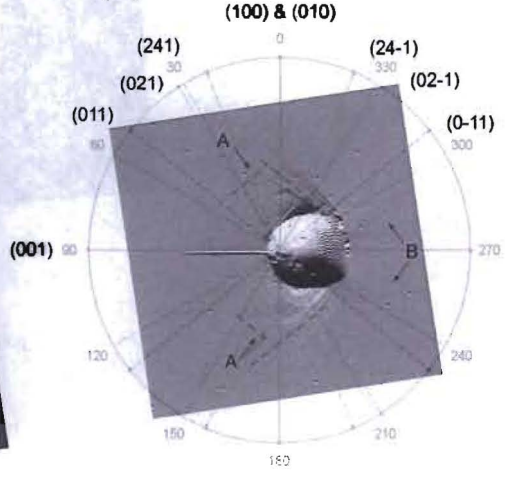

(d.)

Figure 5. Indenter tip SPM deflection images of (001) impressions at loads: 7 μm (a.) 1.25 mN (b.) 3.5 mN (c.) 5 mN

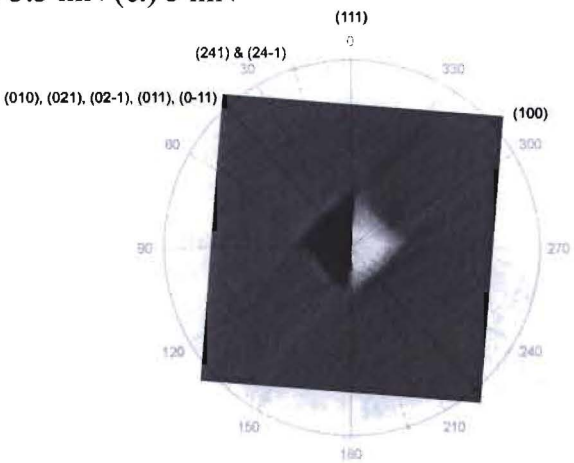

(a.)

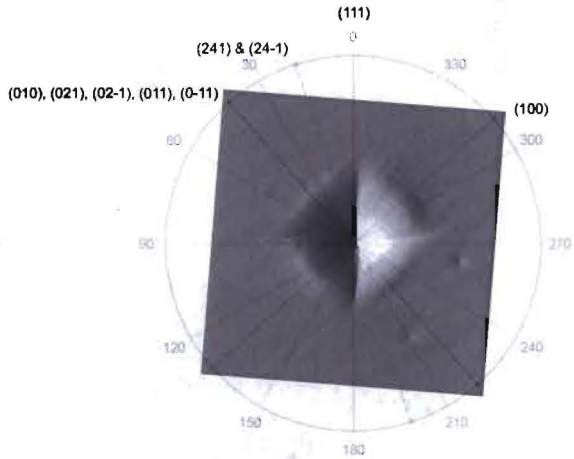

(b.)

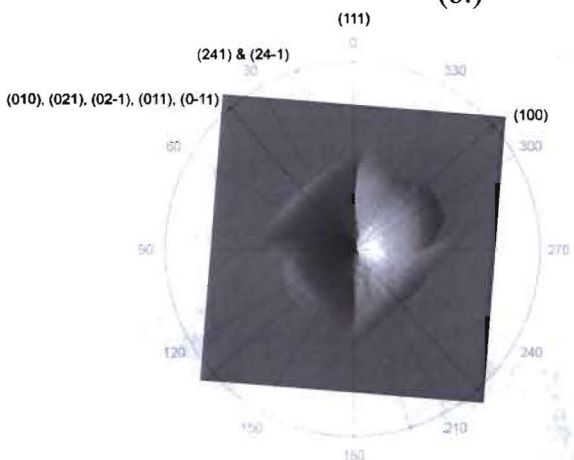

(c.)

Figure 6. Indenter tip SPM of impressions: (a.) (001) RDX, 7 μm deflection and height images and (b.) aluminum, 10 μm deflection and height images

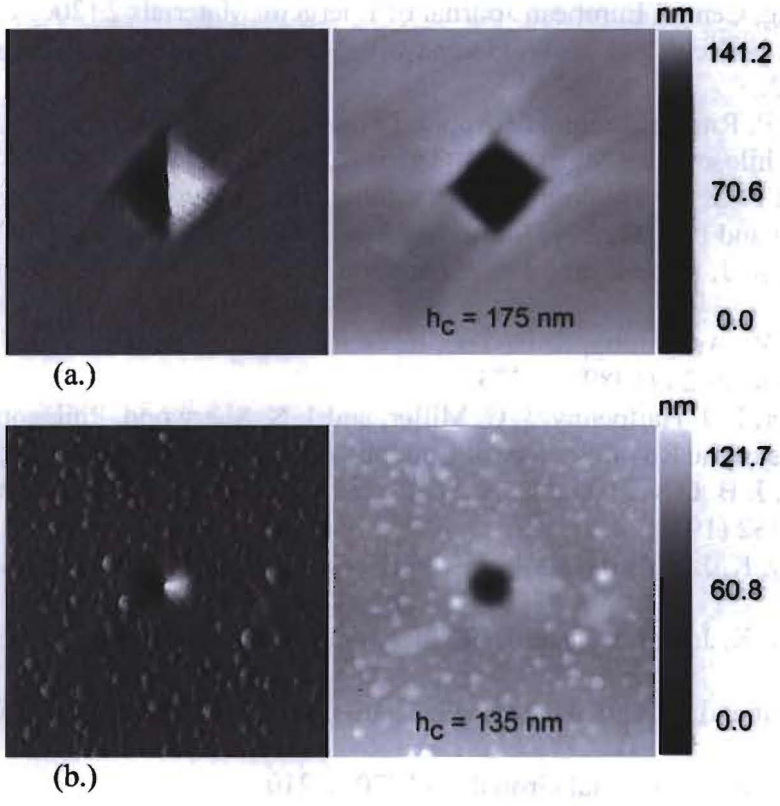

Figure 7. AFM deflection image of (021) impression with zone axes overlaid: 4 mN load, 10 μm

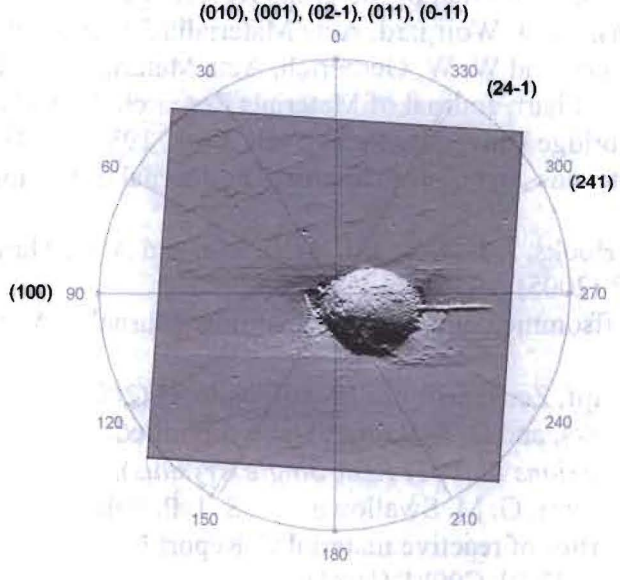

References

[1] C. S. Choi and E. Prince, Acta Crystallographica B28 (1972) p.2857.
[2] R. W. Armstrong, Central European Journal of Energetic Materials 2 (2005) p.55.
[3] S. M. Walley, J. E. Field, and M. W. Greenaway, Materials Science and Technology 22 (2006) p.402.
[4] J. J. Dick and J. P. Ritchie, Journal of Applied Physics 75 (1994) p.2728.
[5] S. Amelinckx, Philosophical Magazine 1 (1956) p.269.
[6] W. Connick and F. G. J. May, Journal of Crystal Growth 5 (1969) p.65.
[7] I. T. McDermott and P. P. Phakey, Journal of Applied Crystallography 4 (1971) p.479.
[8] P. J. Halfpenny, K. J. Roberts, and J. N. Sherwood, Journal of Materials Science 19 (1984) p.1629.
[9] W. L. Elban, R. W. Armstrong, K. C. Yoo, R. G. Rosemeier, and R. Y. Yee, Journal of Materials Science 24 (1989) p.1273.
[10] H. G. Gallagher, P. J. Halfpenny, J. C. Miller, and J. N. Sherwood, Philosophical Transactions of the Royal Society of London A 339 (1992) p.293.
[11] C. A. Brookes, J. B. O'Neill, and B. A. W. Redfern, Proceedings of the Royal Society of London A. 332 (1971) p.73.
[12] P. J. Halfpenny, K. J. Roberts, and J. N. Sherwood, Journal of Crystal Growth 69 (1984) p.73.
[13] P. J. Halfpenny, K. J. Roberts, and J. N. Sherwood, Philosophical Magazine A. 53 (1986) p.531.
[14] I. T. McDermott and P. P. Phakey, Physica status solidi. A: Applied research 8 (1971) p.505.
[15] K. A. Gross, Journal of Crystal Growth 6 (1970) p.210.
[16] H. Klapper, R. A. Becker, D. Schmiemann, and A. Faber, Crystal research and technology 37 (2002) p.747.
[17] K. J. Ramos and D. F. Bahr, Journal of Materials Research 22 (2007) p.2037.
[18] Y. Gaillard, C. Tromas, and J. Woirgard, Acta Materialia 54 (2006) p.1409.
[19] D. F. Bahr, D. E. Kramer, and W. W. Gerberich, Acta Materialia 46 (1998) p.3605.
[20] W. C. Oliver and G. M. Pharr, Journal of Materials Research 7 (1992) p.1564.
[21] K. L. Johnson, (Cambridge University Press, New York, 1985), p. 93.
[22] J. J. Haycraft, L. L. Stevens, and C. J. Eckhardt, The Journal of Chemical Physics 124 (2006) p.024712.
[23] R. B. Schwarz, D. E. Hooks, J. J. Dick, J. I. Archuleta, and A. R. Martinez, Journal of Applied Physics 98 (2005) p.056106.
[24] W. L. Elban, J. C. Hoffsommer, and R. W. Armstrong, Journal of Materials Science 19 (1984) p.552.
[25] M. Goken and M. Kempf, Zeitschrift Fur Metallkunde 92 (2001) p.1061.
[26] K. J. Ramos, D. E. Hooks, and D. F. Bahr, (To be submitted: *Defect and surface asperity dependent load-excursions in (001) RDX Single Crystals*).
[27] J. E. Field, M. M. Chaudhri, G. M. Swallowe, and S. J. P. Palmer, "Deformation, fracture and explosive properties of reactive materials," Report No. Office of Naval Research Interim Report, DAJA37-81-C0081 (1981).

[28] J. R. Rae, D. E. Hooks, and L. C., in *The stess versus strain response of single β-HMX crystals in quasi-static compression*, Norkfolk, VA, 2006.
[29] G. W. Groves and A. Kelly, Philosophical Magazine 8 (1963) p.877.
[30] U. F. Kocks, Philosophical Magazine 10 (1964) p.187.
[31] J. P. Hirth and J. Lothe, *Theory of Dislocations, 2nd ed.*, Krieger, Malabar, FL, 1982.
[32] S. A. S. Asif and J. B. Pethica, Philosophical Magazine A76 (1997) p.1105.
[33] A. B. Mann and J. B. Pethica, Applied Physics Letters 69 (1996) p.907.
[34] C. A. Schuh, J. K. Mason, and A. C. Lund, Nature Materials 4 (2005) p.617.
[35] D. F. Bahr and G. Vasquez, Journal of Materials Research 20 (2005) p.1947.
[36] N. Gane, Proceedings of the Royal Society of London A. 317 (1970) p.367.
[37] A. E. H. Love, Quarterly Journal of Applied Mathematics 10 (1939) p.161.
[38] J. G. Swadener and G. M. Pharr, Philosophical Magazine A. 81 (2001) p.447.
[39] J. J. Vlassak and W. D. Nix, Journal of the Mechanics and Physics of Solids 42 (1994) p.1223.
[40] W. L. Elban and R. W. Armstrong, in *Microhardness study of RDX to assess localized deformation and its role in hot spot formation*, 1982, p. 976.
[41] F. W. Daniels and C. G. Dunn, Transactions of the American Society for Metals 41 p.419.
[42] P. M. Sargent and T. F. Page, Journal of Materials Science 20 (1985) p.2388.
[43] Y. Gaillard, C. Tromas, and J. Woirgard, Acta Materialia 51 (2003) p.1059.
[44] H. G. Gallager, P. J. Halfpenny, and J. C. Miller, Philosophical Transactions of the Royal Society of London A 339 (1992) p.293.